PHYSICAL REVIEW APPLIED **17,** 064036 (2022)

# Electrically Modulated Wavelength-Selective Photodetection Enabled by $MoS_2/ZnO$ Heterostructure

Kishan Lal Kumawat,[1,‡] Pius Augustine,[1,2,‡] Deependra Kumar Singh,[1,3] Karuna Kar Nanda,[1,3,4,*]
and Saluru Baba Krupanidhi[1,†]

[1] *Materials Research Centre, Indian Institute of Science, Bangalore 560012, India*
[2] *Materials Research Laboratory, Sacred Heart College (Autonomous), Thevara, Kochi 682013, India*
[3] *Institute of Physics, Bhubaneswar 751005, India*
[4] *Homi Bhabha National Institute, Mumbai 400094, India*

(Received 18 October 2021; revised 23 April 2022; accepted 24 May 2022; published 21 June 2022)

Regardless of the significant progress in photodetectors (PDs), most conventional technologies are equipped with optical filters for spectral discrimination, which results in expensive circuitry as well as a high incidence of energy loss. Different from traditional PDs, a $MoS_2/ZnO$ heterostructure-based PD is demonstrated that exhibits a bias-dependent switchable spectral response. A low-band-gap $MoS_2$ thin film is vertically stacked on top of a high-band-gap ZnO film that allows selective charge transport from each layer by modulating the applied bias, resulting in a fine discrimination between visible and near-infrared (NIR) light. Under a lower applied bias, a dominant photoresponse in the visible region by the ZnO film is observed, whereas an enhanced response in the NIR region is obtained at higher bias, which is attributed to the generation of charge carriers in the $MoS_2$ region. The excellent figures of merit obtained in the study attest to the high quality of the device, paving the way for fabricating energy-efficient imaging systems free of optical filters.

DOI: 10.1103/PhysRevApplied.17.064036

## I. INTRODUCTION

Photodetectors (PDs) are the sensors that detect incoming light signals, thus, finding their applications in diverse areas, including biological detection [1,2], image sensing [3,4], optical and space communications [5], remote controls, and environmental monitoring [6]. Based on the spectral detection range displayed by the device, PDs are categorized as narrowband and broadband [7]. Narrowband PDs are required for specified wavelength detection, especially in the areas of missile and defense technology, whereas broadband PDs are widely in demand for multicolored light detection [8]. Several strategies are explored to achieve narrowband detection, which include (i) the use of optical band-pass filters on photodetectors, (ii) the employment of a semiconductor material with narrowband absorption in the device, and (iii) exploitation of the charge-collection-narrowing mechanism [9]. Many reported photodetectors use optical filters for spectral discrimination, which makes the device more bulky and less efficient due to the loss in incident-light energy [10]. So, technology that facilitates multispectral photodetection in a single device without an optical filter would be highly beneficial. Single narrowband PDs are limited to detection over a specific spectral range, which hampers their spectral selectivity and the resolution of the image [11,12]. Better object identification through the processing of multiple waveband signals with a single camera is a challenging task. Hence, broadband detection along with wavelength discrimination is highly desirable.

So far, dual or multiple waveband detection has been achieved by fabricating epitaxial multiple-absorber layers with different band-gap semiconductor [13], alloy [14], and superlattice heterostructures [15]. However, the deposition of multiple semiconductor layers leads to additional challenges like thermal and lattice mismatches between the semiconductor layers, limiting their absolute performance [16–19]. Recently, Su *et al.* presented dual-color UV photodetection in a dual-phase Be-ZnO alloy with an asymmetric Ti/Au metal-contact-based device [14]. However, the device performance was limited to the near-UV (330 nm) to mid-UV (240 nm) region only. Deng *et al.* integrated the $MoS_2$ layer with (In, Al)As and (In, Ga)As with a complicated $MoS_2/In_{0.52}Al_{0.48}As/Si$ ($\delta$-doping)/$In_{0.52}Al_{0.48}$ $As/In_{0.53}Ga_{0.47}As/(In, Al)As$ composition to attain visible near-infrared (NIR) dual-color detection through barrier height generation by introducing

---

[*] nanda@iisc.ac.in

[†] sbk@iisc.ac.in

[‡] Kishan Lal Kumawat and Pius Augustine contributed equally to this work.

(In, Al)As between $MoS_2$ and (In, Ga)As [20]. Hence, a photodetector with a stable and simple device architecture with broadband detection needs to be fabricated.

In recent years, transition-metal dichalcogenides have been extensively explored due to their excellent optoelectronic properties [21]. Particularly, $MoS_2$ has attracted special attention due to its *n*-type semiconductor behavior, high charge-carrier mobility, and strong light-matter interaction range (visible-NIR) with excellent stability and an ultrafast response [22–26]. Furthermore, the absence of dangling bonds at the surface of $MoS_2$ overcomes the constraints of lattice mismatches and facilitates integration with wide-band-ap semiconductors, such as ZnO, SiC, AlN, and GaN, with fewer interfacial defects [27,28]. Among wide-band-gap semiconductors, ZnO is a widely exploited semiconductor that is frequently used to develop UV photodetectors [29–31] due to its wide band gap of about 3.4 eV, low-cost device fabrication with high-quality thin films, and excellent thermal and chemical stability [32–34]. Therefore, the integration of $MoS_2$ with a large-band-gap semiconductor like ZnO seems to be a practical approach to develop a dual-color (UV-NIR) photodetector device. Here, we present a simple yet effective $MoS_2/ZnO$-based broadband photodetector device, which exhibits electrically modulated dual-color detection in the range of visible to NIR.

Integration of the two *n*-type semiconductors ($MoS_2$ and ZnO) intrinsically generates an electron barrier height at the heterojunction interface, thus blocking the majority charge carrier from flowing through the generated large depletion region. The device exhibits enhanced detection near a wavelength of 400 nm with a negligible response from the higher-wavelength region at lower applied bias (<2 V) and improved photodetection of the NIR region (900 nm), with complete elimination of visible-wavelength detection, at higher applied bias. The responsivity is determined to be 4.56 $AW^{-1}$ (400 nm) and $6.04 \times 10^3$ $AW^{-1}$ (900 nm) at 1.0 and 8.0 V, respectively. Overall, this study opens opportunities to utilize the highly responsive and cost-effective $MoS_2/ZnO$ heterostructure for bias-modulated visible-NIR spectral detection.

## II. EXPERIMENTAL SECTION

### A. Device fabrication

The $MoS_2/ZnO$ heterostructure is prepared in a two-step process. In the first step, Zn metal is sputtered on commercially procured Si wafers (Graphene Supermarket). Sputtering is carried out at a working pressure of $4 \times 10^{-3}$ mbar under 1.5-sccm argon flow for 4 min (power = 45 W). A wafer with the sputtered Zn layer is heated to 500 °C for 3 h at ambient pressure to realize the ZnO film, which acts as the substrate for the deposition of $MoS_2$. In the second step, a $MoS_2$ thin film on ZnO is deposited using pulsed laser deposition (PLD) [35–37]. After loading the ZnO film and $MoS_2$ target, the PLD chamber (Excel Instruments) is evacuated to a base pressure of $3.3 \times 10^{-6}$ mbar. The substrate is heated to 700 °C and preannealed for 40 min to avoid thermal stress on the ZnO/Si substrate. During deposition of the $MoS_2$ layer, a KrF excimer laser (248 nm and 10-ns pulse width) is used as the ablation source. The energy of the laser beam is set to be 300 mJ at 3-Hz repetition rate, and ablation is carried out using a focused laser beam of 300 shots on a rotating target. The plasma thus produced is deposited on the ZnO film, which is kept at a perpendicular distance of 4.5 cm away from the target. After laser ablation, the film thus formed is annealed inside the chamber at the deposition pressure and temperature for 40 min to realize the $MoS_2$ thin film. Circular electrodes of silver with a diameter of 0.4 mm are evaporated on the $MoS_2$ and ZnO layers on either side of the heterojunction by thermal evaporation to permit electrical measurements to be made.

### B. Characterization

X-ray diffraction (XRD) patterns are recorded using a Bruker D8 diffractometer (Cu K$\alpha$ source). The $\mu$-Raman spectrum of the $MoS_2$ film is recorded using a Lab RAM HR instrument equipped with a 532-nm laser, and diffuse reflectance spectra (DRS) are recorded using a Perkin Elmer Lambda 750 UV-vis NIR spectrophotometer. ULTRA 55 scanning electron microscopy (SEM) is used to determine the morphology of $MoS_2$. The thickness of various films is measured using A100 APE Research atomic force microscopy (AFM). Compositional analysis of the films is carried out using AXIS ULTRA x-ray photoelectron spectroscopy (XPS). Current ($I$)-voltage ($V$) characteristics are studied using a Keithley 2400 source meter, and the photoresponse is analyzed using Oriel's QEPVSI system attached to a 300-W xenon bulb. The output power density in the range from 0.1 to 0.0125 $mW/cm^2$ is calibrated to study the photoresponse at various input-light powers. A computer-controlled and wavelength-adjustable monochromator in the range of 300–1200 nm is used to determine the spectral response exhibited by the device.

## III. RESULT AND DISCUSSION

### A. Structural and optical analysis

The phase formation of ZnO and $MoS_2$ is confirmed by XRD and Raman spectroscopy, respectively. UV-vis spectra are obtained to determine their band gaps. Figure 1(a) presents the XRD pattern (blue) of the as-deposited ZnO thin film. The XRD pattern matches well with ICSD collection code no. 230510 (red), revealing the hexagonal wurtzite crystal structure of ZnO [38]. The Raman spectrum of $MoS_2$ [see Fig. S1(a) within the Supplemental Material [56] for detailed Raman spectra] reveals peaks

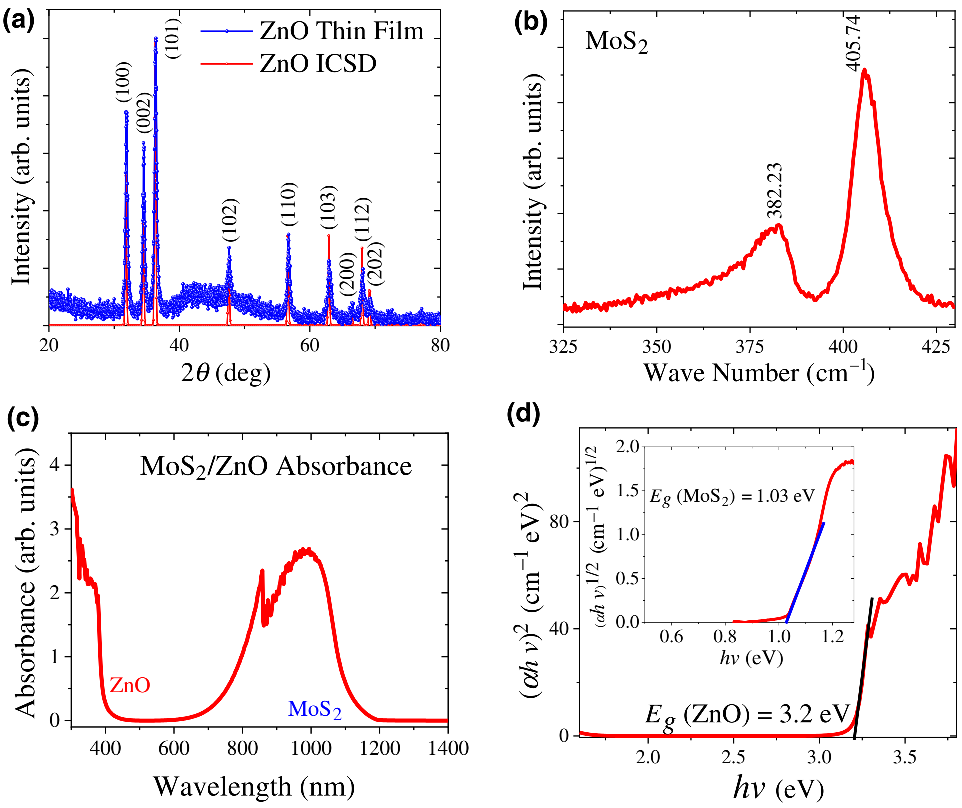

FIG. 1. (a) XRD pattern of ZnO film. (b) Raman spectrum of $MoS_2$. (c) Absorbance spectrum of $MoS_2/ZnO$ heterostructure. (d) Tauc plots for ZnO and $MoS_2$ (inset).

with a dominant $2H$ $MoS_2$ phase over the $1T$ phase. The presence of the small $1T$ phase of $MoS_2$ suggests that there are some sulfur vacancies in $MoS_2$. The Raman spectrum [Fig. 1(b)] depicts the two characteristic peaks of $MoS_2$ at 382.23 ($E_{2g}^1$ mode) and 405.74 $cm^{-1}$($A_{1g}$ mode) [39,40]. The $A_{1g}$ mode corresponds to the out-of-plane vibration of S atoms, while the in-plane vibrations of Mo and S atoms are indexed to $E_{2g}^1$. The wave-number difference of 23.51 $cm^{-1}$ signifies the multilayer growth of $MoS_2$ [24,41].

To determine the optical band gaps of $MoS_2$ and ZnO, the DRS is recorded [see Fig. S1(b) within the Supplemental Material [56] for DRS spectra]. The Kubelka-Munk (KM) function is used to convert the DRS into an absorption spectrum. The KM function [42] is given as $F(R_{\mathrm{Infinite}}) = \alpha/S = (1-R)^2/2R$, where $R$ is the relative reflectance of the film; $\alpha$ and $S$ are the absorbance and scattering coefficients, respectively. The scattering coefficient is almost independent of the energy, so the KM function is equal to the absorption coefficient. Figure 1(c) shows the absorbance spectrum of the $MoS_2/ZnO$ thin film. Two major peaks are observed at 280 and 986 nm, corresponding to the ZnO- and $MoS_2$-band absorptions, respectively. Therefore, the direct band gap of ZnO is determined using a Tauc plot [Fig. 1(d)] by plotting the graph of $(\alpha h\upsilon)^2$ versus $h\upsilon$. Since multilayer $MoS_2$ is an indirect-band-gap semiconductor, its optical band gap is determined by plotting the curve of $(\alpha h\upsilon)^{1/2}$ versus $h\upsilon$ [inset of Fig. 1(d)]. The band gaps are found to be 3.2 and 1.03 eV for ZnO and $MoS_2$, respectively.

The thicknesses of Zn, ZnO, and $MoS_2$ are determined by AFM [see Figs. S2(a)–S2(c) within the Supplemental Material [56] for AFM images] and are found to be 100, 133, and 6.57 nm, respectively. The morphology of as-deposited $MoS_2$ is characterized by SEM. Figure 2(a) shows that $MoS_2$ forms a continuous film with granular morphology. Figure 2(b) depicts the wide XPS spectrum of the $MoS_2/ZnO$ heterostructure, which reveals the presence of Mo, S, Zn, and O elements in the heterostructure [43]. Figure 2(c) shows the high-resolution spectrum of Mo $3d$. The peaks at 229.04 ($3d_{5/2}$) and 232.2 eV ($3d_{3/2}$) correspond to the +4 oxidation state of Mo, while the weak shoulder at 235.52 eV corresponds to the +6 oxidation state of Mo [44,45]. The other shoulder peak at 226.6 eV is characteristic of Mo—S bonding. Also, a doublet is observed at 163.10 and 161.90 eV in the S $2p$ spectrum [Fig. 2(d)] [46]. The difference between the two peaks is 1.2 eV, which confirms the formation of $MoS_2$. Overall, XPS studies validate the formation of $MoS_2$. The stoichiometry of $MoS_2$ is determined by CASA XPS software. The atomic percentages of Mo and S are found to be 35.3% and 64.7%, indicating the Mo:S ratio to be 1:1.83.

### B. Electrical studies

Figure 3(a) shows a schematic of the $MoS_2/ZnO$ heterostructure with Ag as the top contacts. $I$–$V$

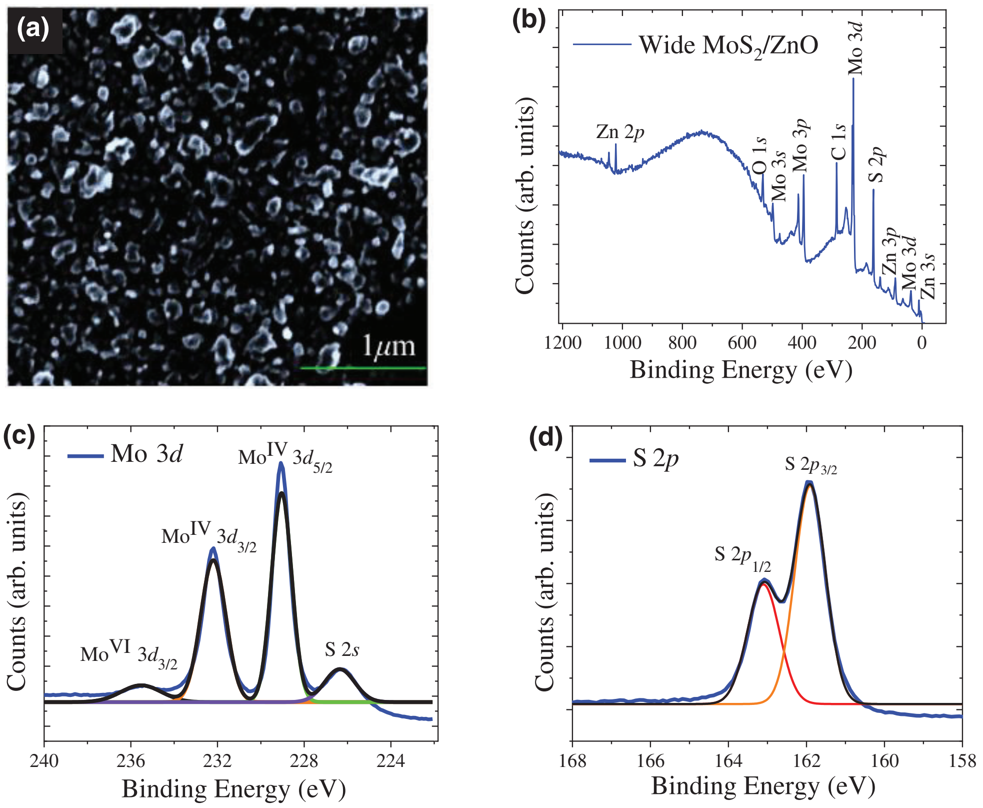

FIG. 2. (a) SEM image of as-deposited $MoS_2$. (b) XPS survey spectrum of $MoS_2/ZnO$ heterostructure. High-resolution XPS spectra of (c) Mo 3*d* and (d) S 2*p*.

characteristics of the $MoS_2/ZnO$ heterostructured device are examined under illumination with different wavelengths of light in the range of 400–1200 nm [see Fig. S3(a) within the Supplemental Material [56] for *I*–*V* characteristics]. It is observed that Ag forms ohmic contacts with both ZnO and $MoS_2$, as evidenced from the dark current-voltage characteristics. Interestingly, a significant change in current is observed in the positive-bias region when irradiated with photons. Figure 3(b) presents the *I*–*V* characteristics in the applied positive bias. It is evident that, under lower applied biases (<2.0 V), the sensitivity in the visible range (<600 nm) is prominent, while the response in the NIR region is prominent at higher bias with a crossover around 2.5 V [see Fig. S3(b) within the Supplemental Material [56] for a magnified view of the *I*-*V* plot around 2 V].

To further understand the photoresponse of the device, the spectral response is observed over a wide range of wavelengths. Figure 4 demonstrates the spectral response of the $MoS_2/ZnO$ heterostructure at different applied biases. It is obvious from Fig. 4(a) that the photocurrent is predominant at 400 nm for an applied bias of 1 V, while it is negligible at other wavelengths. As the applied bias is increased in steps, it is found that [see Figs. S4(a) and S4(b) within the Supplemental Material [56] for current-time plots] the photocurrent in the NIR region demonstrates a gradual increase, and the NIR photoresponse surpasses the visible response at an applied bias of 2.5 V, as shown in Fig. 4(b).

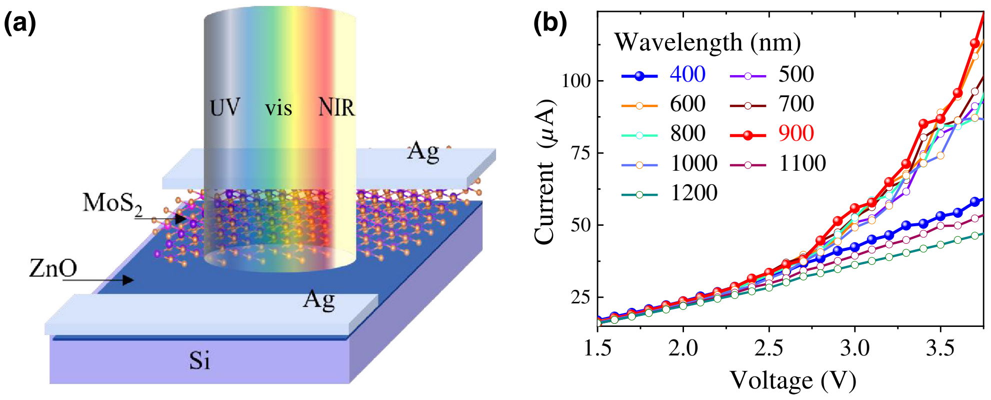

FIG. 3. (a) Schematic of the $MoS_2/ZnO$ heterostructured device. (b) *I-V* characteristics under illumination with light of wavelengths from 400 to 1200 nm.

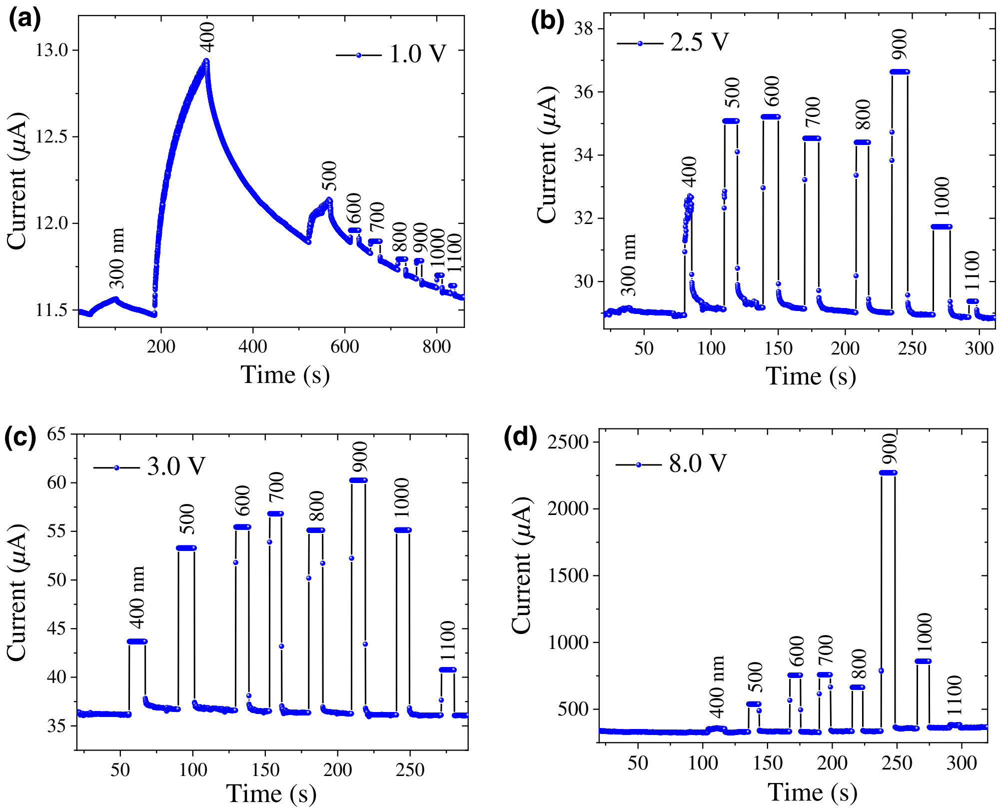

FIG. 4. Spectral response exhibited by the $MoS_2/ZnO$ heterostructured device under different wavelengths of illuminated light at an applied bias of (a) 1.0 V, (b) 2.5 V, (c) 3.0 V, and (d) 8.0 V.

With a further increase in the bias [Fig. 4(c) depicts the response under an applied bias of 3.0 V and see Figs. S4(c) and S4(d) within the Supplemental Material [56] for the photoresponse under applied biases of 5.0 and 7.0 V], the photoresponse in the visible region is completely suppressed and the device displays a substantial improvement in the NIR photoresponse, which is apparent in Fig. 4(d) (response at an applied bias of 8.0 V). It can be elucidated that, by and large, the device shows a response at 900-nm light at 8.0 V, while the response in the visible region is substantially lower. Overall, one can have dual-color photodetection, ranging from visible to NIR, by electrical modulation and broadband photodetection.

Apart from electrical modulation of the photoresponse, it can also be noted that the response and recovery times are also dependent on the applied bias. The faster response at higher biases could be ascribed to two main reasons: (1) bias enhancement across the heterostructure enables effective separation of the photogenerated electron-hole pair and its enhanced transportation to the electrodes, and/or (2) the NIR photoresponse is mainly observed due to the absorbance of light by $MoS_2$, as its band gap is around 1.03 eV, and demonstrates a faster response due to high charge-carrier mobility.

Responsivity, detectivity, sensitivity, and response time are the figures of merit that proclaim the quality of the photodetector. The responsivity ($R$) is measured as the ratio of the generated photocurrent to the incident-light power [47]; this can be represented as

$$R = I_{\text{ph}}/(PA),$$

where $I_{\text{ph}}$ is the generated photocurrent ($I_{\text{light}}$–$I_{\text{dark}}$) upon illumination with light; $P$ is the incident-light intensity; and $A$ is the effective area of the device, which is 0.0032 $\text{cm}^2$ in our case. Detectivity ($D$*) [48] is a measure of the ability of the device to detect the lowest-possible light signal falling on the device and is calculated by

$$D^{*} = R/(2qJ_d)^{1/2},$$

where $R$ is the responsivity, $q$ represents the electronic charge ($1.602 \times 10^{-19}$ C), and $J_d$ is the dark-current density of the detector. Sensitivity [49] is defined as the ratio of generated photocurrent ($I_{\text{ph}}$) to the dark current ($I_d$). Sensitivity is calculated using the equation $S = I_{\text{ph}}/I_d$. The response time [50] is the time taken by the detector to increase the photocurrent from 10% to 90% of the maximum photocurrent generated, and the recovery time is the time taken for the decay of the photocurrent from 90% to 10%, when the illuminated light is turned off.

Figure 5(a) presents the spectral response of the device under different applied biases (1.0–2.5 V). The responsivity calculated under applied biases up to 2.0 V is found to be higher for the 400-nm wavelength, while it is lower in the NIR region of light illumination. The photoresponse

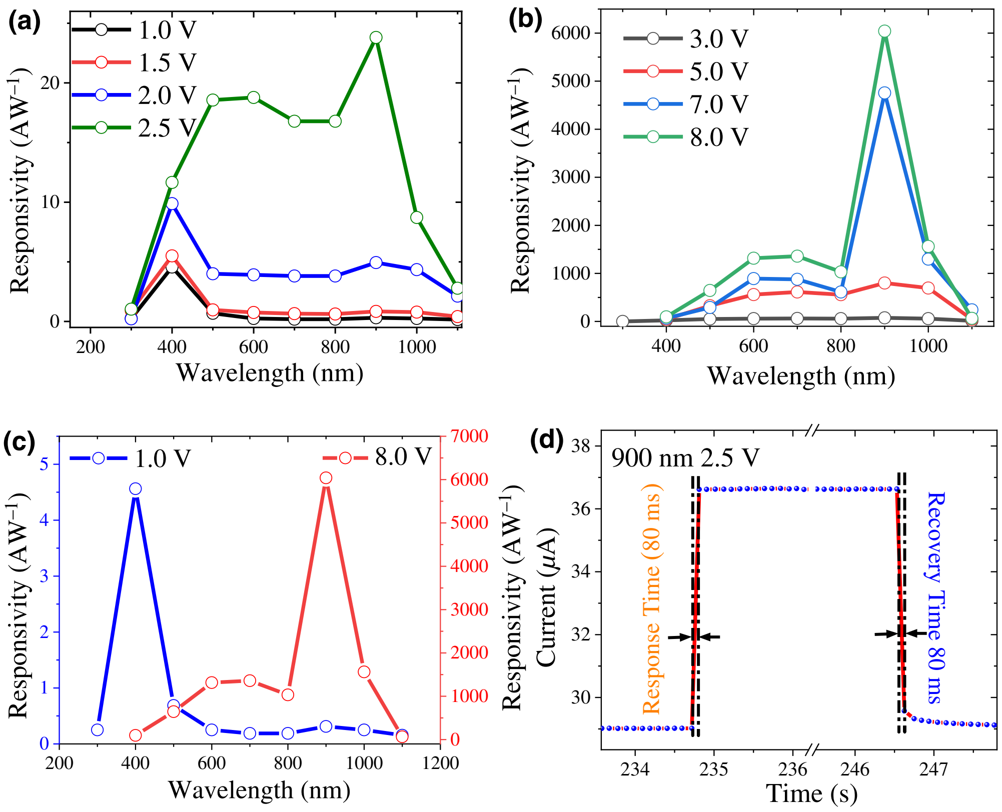

FIG. 5. Variation of responsivity with illuminated-light wavelength at (a) low applied biases, (b) high applied biases, and (c) 1.0 at and 8.0 V. (d) Response and recovery times under 900-nm light at 2.5 V.

displays a gradual increase in the NIR region, while it starts to decrease in the visible region beyond 2.5 V [Fig. 5(b)]. Figure 5(c) shows the responsivity variation at higher values of applied bias, which also confirms the earlier obsrevation, i.e., a visible response at an applied bias of 1.0 V, but a NIR response at 8.0 V, and the responsivity values are 4.56 AW$^{-1}$ (400 nm at 1.0 V) and 6.04 × 10$^3$ AW$^{-1}$ (900 nm at 8.0 V), respectively. Responsivity is observed to increase with an increase in the applied bias at each wavelength. This is because of the effective seperation of the photogenerated electron-hole pair and its enhanced transportion to the respective electrode, which results in a high photocurrent at higher applied bias. Figure 5(d) depicts the photocurrent versus time graph to determine the

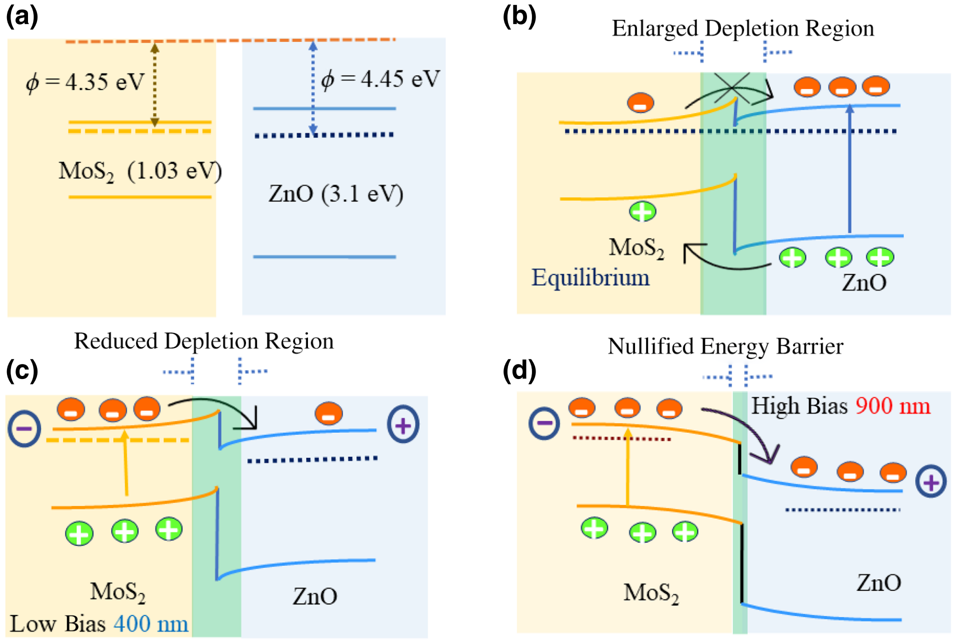

FIG. 6. (a) Energy-band diagram of the MoS$_2$/ZnO heterostructure before formation of the heterointerface. Band alignment of independent layers at (b) equilibrium, (c) low bias under illumination of 400-nm light, and (d) at high bias under illumination of 900-nm light.

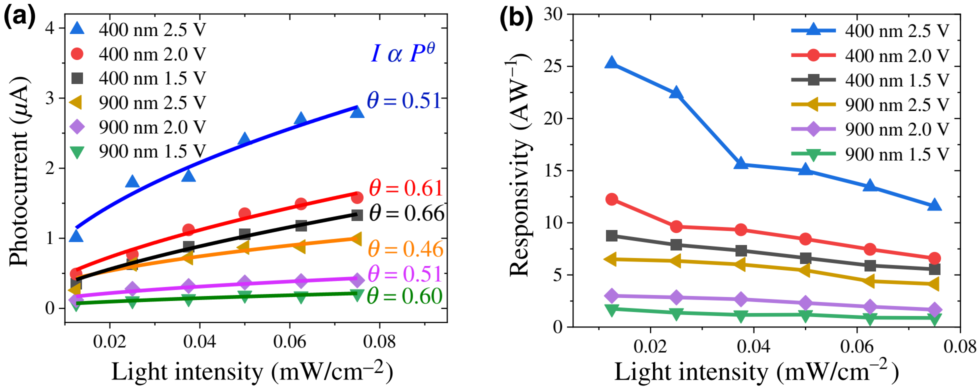

FIG. 7. Variation of (a) photocurrent and (b) responsivity with illuminated light intensity at different biases and wavelengths of light.

response and recovery times of the device. Both response and recovery times are determined to be 80 ms under the illumination of 900-nm light at the crossover bias; these values provide evidence that the device is able to detect rapidly changing optical signals.

Figure 6 demonstrates the energy-band diagram of the $MoS_2/ZnO$ heterostructure at different applied biases. Figure 6(a) shows the band alignment before the formation of a heterointerface between the two materials. The work functions ($\phi$) of $MoS_2$ and ZnO are taken as 4.35 and 4.45 eV, respectively, from the literature [51–53]. When these two materials form a heterostructure, a junction barrier with a large depletion region emerges at the junction [Fig. 6(b)], which restricts the transport of majority charge carriers (electrons) from $MoS_2$ to ZnO. As we apply a forward bias, the depletion region width starts to contract, resulting in a reduced barrier height [Fig. 6(c)]. However, at low biases, the major contribution to the photocurrent is electrons and holes generated at the ZnO side of the heterostructure. High-energy photons excite the electrons from the valence band to the conduction band of ZnO. Although high-energy photons can also excite electrons in $MoS_2$, the contribution to the photocurrent is expected to be low, as the excited electrons generate phonons and are recombined with holes. On the other hand, a low photoresponse in the NIR region is believed to be due to the existence of a tunneling barrier at the $ZnO/MoS_2$ interface. The electrons present in the conduction band of $MoS_2$ would be able to tunnel through the barrier and go into the conduction band of ZnO, yielding a low photoresponse in the NIR region at low bias. With a further increase in the applied bias, the width of the depletion barrier contracts significantly, as shown in Fig. 6(d), and nullifies the energy barrier at the interface; therefore, the maximum number of generated electrons from $MoS_2$ reach the ZnO region, causing a considerable increase in the NIR photoresponse at higher bias. Because of the rapid response of $MoS_2$ to the incident light, compared with ZnO, the effect of the ZnO response is reasonably nullified by the enhanced photoresponse, which arises due to the large number of generated carriers reaching the external circuit from the $MoS_2$ layer.

Figure 7(a) shows the dependence of the photocurrent on power density with different applied biases and light wavelengths. The photocurrent is fitted with the power-law equation, $I_{ph} \propto P^{\theta}$, where $I_{ph}$ is the photocurrent, $P$ is the illuminated power density in $mW/cm^2$ and $\theta$ is the photoresponse-related exponent parameter. The value of $\theta$ is found to be 0.51, 0.61, and 0.66 for an applied bias of 2.5, 2.0, and 1.5 V, respectively, under 400-nm light (see Fig. S5 within the Supplemental Material [56] for a log $I$ vs log $P$ plot) and is 0.46, 0.51, and 0.60 under 900-nm light. The less-than-unity values of $\theta$ suggest that photocurrent generation is due to a complex process of trapping and recombination of charge carriers [54]. Also, it is observed that, with increasing applied bias, the value of $\theta$ is decreases, which could be attributed to the loss of electrons due to the presence of defect states and associated recombination at a particular applied bias. Figure 7(b) shows the variation of the device responsivity under different illuminated power densities with different applied biases and light wavelengths. Also, it is observed that, while responsivity displays a positive trend with applied bias, it shows a decline in value with increasing intensity of light illumination. At higher light intensities, the recombination of charge carriers and their scattering dominate over the rate of generation of charge carriers and their transportation to the electrodes. Hence, the responsivity is low at higher light intensities. However, with increasing bias, the responsivity of the device increases due to better charge separation and the fast transportation of electrons and holes to the electrodes [24,55]. Detectivity also follows the same trend as responsivity and is attributed to a very small change in the dark current with applied bias [see Fig. S6(a) within the Supplemental Material [56] for variation in detectivity with light intensity]. However, the sensitivity increases with increasing intensity as well as applied bias [see Fig. S6(b) within the Supplemental

Material [56] for sensitivity vs light intensity]. This is because of the increase in photocurrent with respect to dark current under the applied bias and the intensity of incident light.

## IV. CONCLUSIONS

A simple yet effective $MoS_2/ZnO$ heterojunction is fabricated by pulsed laser deposition and dc sputtering. The device shows electrically modulated dual-color photodetection in the visible and NIR regions. The device exhibits a largely visible photoresponse at 1.0 V, while it is NIR at 8.0 V, and the responsivity values are 4.56 $AW^{-1}$ (400 nm) and $6.04 \times 10^3$ $AW^{-1}$ (900 nm), respectively. The results reveal that the $MoS_2/ZnO$ hetrostructure could be a suitable candidate for a low-cost and optical-filter-free wavelength-selective photodetector.

## ACKNOWLEDGMENTS

K.K.N. and P.A. are thankful to the Science and Engineering Research Board (SERB), Department of Science and Technology (DST), Government of India, for the TARE grant (Grant No. TAR/2020/000241). The authors thank Sudeeksha and Rakesh from the HORIBA-IISc Technical Center for Raman measurements. D.K.S. is thankful to the Council of Scientific and Industrial Research, Government of India, New Delhi, for providing a senior research fellowship and the Indian Institute of Science, Bangalore, India, for providing an RAship. S.B.K. acknowledges support from an INSA senior scientist fellowship.

[1] H. Shi, Z. Zhang, S. Pirandola, and Q. Zhuang, Entanglement-Assisted Absorption Spectroscopy, Phys. Rev. Lett. **125**, 180502 (2020).

[2] F. Cao, J. Chen, D. Yu, S. Wang, X. Xu, J. Liu, Z. Han, B. Huang, Y. Gu, K. L. Choy, and H. Zeng, Bionic detectors based on low-bandgap inorganic perovskite for selective NIR-I photon detection and imaging, Adv. Mater. **32**, 1905362 (2020).

[3] H. Shekhar, A. Fenigstein, T. Leitner, B. Lavi, D. Veinger, and N. Tessler, Hybrid image sensor of small molecule organic photodiode on CMOS – integration and characterization, Sci. Rep. **10**, 7594 (2020).

[4] R. Meyers, K. S. Deacon, and Y. Shih, Ghost-imaging experiment by measuring reflected photons, Phys. Rev. A **77**, 041801 (2008).

[5] M. Kumar, J.-Y. Park, and H. Seo, High-performance and self-powered alternating current ultraviolet photodetector for digital communication, ACS Appl. Mater. Interfaces **13**, 12241 (2021).

[6] C. Dincer, R. Bruch, E. Costa-Rama, M. T. Fernández-Abedul, A. Merkoçi, A. Manz, G. A. Urban, and F. Güder, Disposable sensors in diagnostics, food, and environmental monitoring, Adv. Mater. **31**, 1806739 (2019).

[7] M. I. Saidaminov, Md. A. Haque, M. Savoie, A. L. Abdelhady, N. Cho, I. Dursun, U. Buttner, E. Alarousu, T. Wu, and O. M. Bakr, Perovskite photodetectors operating in both narrowband and broadband regimes, Adv. Mater. **28**, 8144 (2016).

[8] R. He, Z. Chen, H. Lai, T. Zhang, J. Wen, H. Chen, F. Xie, S. Yue, P. Liu, J. Chen, and W. Xie, van der Waals transition-metal oxide for vis–MIR broadband photodetection via intercalation strategy, ACS Appl. Mater. Interfaces **11**, 15741 (2019).

[9] J. Wang, S. Xiao, W. Qian, K. Zhang, J. Yu, X. Xu, G. Wang, S. Zheng, and S. Yang, Self-driven perovskite narrowband photodetectors with tunable spectral responses, Adv. Mater. **33**, 2005557 (2021).

[10] H. Kim, W. Kim, Y. Pak, T. J. Yoo, H. W. Lee, B. H. Lee, S. Kwon, and G. Y. Jung, Bias-modulated multicolor discrimination enabled by an organic–inorganic hybrid perovskite photodetector with a p-i-n-i-p configuration, Laser Photonics Rev. **14**, 2000305 (2020).

[11] A. Haddadi, A. Dehzangi, R. Chevallier, S. Adhikary, and M. Razeghi, Bias-selectable nBn dual-band long-/very long-wavelength infrared photodetectors based on $InAs/InAs_{1-x}Sb_x/AlAs_{1-x}Sb_x$ Type-II Superlattices, Sci. Rep. **7**, 3379 (2017).

[12] X. Tang, M. M. Ackerman, M. Chen, and P. Guyot-Sionnest, Dual-band infrared imaging using stacked colloidal quantum dot photodiodes, Nat. Photonics **13**, 277 (2019).

[13] Y. Zhang, A. Haddadi, A. Dehzangi, R. Chevallier, and M. Razeghi, Suppressing spectral crosstalk in dual-band long-wavelength infrared photodetectors with monolithically integrated air-gapped distributed Bragg reflectors, IEEE J. Quantum Electron. **55**, 4000106 (2018).

[14] L. Su, H. Chen, X. Xu, and X. Fang, Novel BeZnO based self-powered dual-color UV photodetector realized via a one-step fabrication method, Laser Photonics Rev. **11**, 1700222 (2017).

[15] L. Li, H. Chen, Z. Fang, X. Meng, C. Zuo, M. Lv, Y. Tian, Y. Fang, Z. Xiao, C. Shan, and Z. Xiao, An electrically modulated single-color/dual-color imaging photodetector, Adv. Mater. **32**, 1907257 (2020).

[16] N. Guo, L. Xiao, F. Gong, M. Luo, F. Wang, Y. Jia, H. Chang, J. Liu, Q. Li, Y. Wu, and Y. Wang, Light-Driven $WSe_2$ -ZnO Junction field-effect transistors for high-performance photodetection, Adv. Sci. **7**, 1901637 (2020).

[17] J.-Y. Wu, Y. T. Chun, S. Li, T. Zhang, J. Wang, P. K. Shrestha, and D. Chu, Broadband $MoS_2$ field-effect phototransistors: Ultrasensitive visible-light photoresponse and negative infrared photoresponse, Adv. Mater. **30**, 1705880 (2018).

[18] X. Wang, P. Wang, J. Wang, W. Hu, X. Zhou, N. Guo, H. Huang, S. Sun, H. Shen, T. Lin, and M. Tang, Ultrasensitive and broadband $MoS_2$ photodetector driven by ferroelectrics, Adv. Mater. **27**, 6575 (2015).

[19] H. Qiao, J. Yuan, Z. Xu, C. Chen, S. Lin, Y. Wang, J. Song, Y. Liu, Q. Khan, H. Y. Hoh, and C. X. Pan, Broadband photodetectors based on graphene-$Bi_2Te_3$ heterostructure, ACS Nano **9**, 1886 (2015).

[20] J. Deng, L. Zong, W. Bao, M. Zhu, F. Liao, Z. Guo, Y. Xie, B. Lu, J. Wan, J. Zhu, and R. Peng, Integration of $MoS_2$

with InAlAs/InGaAs heterojunction for dual color detection in both visible and near-infrared bands, Adv. Opt. Mater. **7**, 1901039 (2019).

[21] S. Mitra, S. Kakkar, T. Ahmed, and A. Ghosh, Graphene-$WS_2$ van der Waals Hybrid Heterostructure for Photodetector and Memory Device Applications, Phys. Rev. Appl. **14**, 064029 (2020).

[22] C. Ko, Y. Lee, Y. Chen, J. Suh, D. Fu, A. Suslu, S. Lee, J. D. Clarkson, H. S. Choe, S. Tongay, and R. Ramesh, Ferroelectrically gated atomically thin transition-metal dichalcogenides as nonvolatile memory, Adv. Mater. **28**, 2923 (2016).

[23] D. Lembke, S. Bertolazzi, and A. Kis, Single-layer $MoS_2$ electronics, Acc. Chem. Res. **48**, 100 (2015).

[24] D. K. Singh, R. Pant, A. M. Chowdhury, B. Roul, K. K. Nanda, and S. B. Krupanidhi, Defect-mediated transport in self-powered, broadband, and ultrafast photoresponse of a $MoS_2$/AlN/Si-based photodetector, ACS Appl. Electron. Mater. **2**, 944 (2020).

[25] F. Urban, F. Giubileo, A. Grillo, L. Iemmo, G. Luongo, M. Passacantando, T. Foller, L. Madauß, E. Pollmann, M. P. Geller, and D. Oing, Gas dependent hysteresis in $MoS_2$ field effect transistors, 2D Mater. **6**, 045049 (2019).

[26] A. Pelella, A. Grillo, F. Urban, F. Giubileo, M. Passacantando, E. Pollmann, S. Sleziona, M. Schleberger, and A. Di Bartolomeo, Gate-controlled field emission current from $MoS_2$ nanosheets, Adv. Electron. Mater. **7**, 2000838 (2021).

[27] K. F. Mak, C. Lee, J. Hone, J. Shan, and T. F. Heinz, Atomically Thin $MoS_2$: A New Direct-Gap Semiconductor, Phys. Rev. Lett. **105**, 136805 (2010).

[28] A. Splendiani, L. Sun, Y. Zhang, T. Li, J. Kim, C. Y. Chim, G. Galli, and F. Wang, Emerging photoluminescence in monolayer $MoS_2$, Nano Lett. **10**, 1271 (2010).

[29] D. Kim and J. Y. Leem, Crystallization of ZnO thin films via thermal dissipation annealing method for high-performance UV photodetector with ultrahigh response speed, Sci. Rep. **11**, 382 (2021).

[30] B. Deka Boruah, Zinc oxide ultraviolet photodetectors: Rapid progress from conventional to self-powered photodetectors, Nanoscale Adv. **6**, 2059 (2019).

[31] S. Liu, M. Y. Li, D. Su, M. Yu, H. Kan, H. Liu, X. Wang, and S. Jiang, Broad-band high-sensitivity ZnO colloidal quantum dots/self-assembled Au nanoantennas heterostructures photodetectors, ACS Appl. Mater. Interfaces **10**, 32516 (2018).

[32] P. S. Huang, F. Qin, and J. K. Lee, Role of the interface between Ag and ZnO in the electric conductivity of Ag nanoparticle-embedded ZnO, ACS Appl. Mater. Interfaces **12**, 4715 (2020).

[33] W. Han, S. Oh, C. Lee, J. Kim, and H. H. Park, ZnO Nanocrystal thin films for quantum-dot light-emitting devices, ACS Appl. Nano Mater. **3**, 7535 (2020).

[34] A. E. Ramírez, M. Montero-Muñoz, L. L. López, J. E. Ramos-Ibarra, J. A. H. Coaquira, B. Heinrichs, and C. A. Páez, Significantly enhancement of sunlight photocatalytic performance of ZnO by doping with transition metal oxides, Sci. Rep. **11**, 2804 (2021).

[35] D. K. Singh, B. Roul, R. Pant, A. M. Chowdhury, K. K. Nanda, and S. B. Krupanidhi, Different types of band alignment at $MoS_2$/(Al, Ga, In)N heterointerfaces, Appl. Phys. Lett. **116**, 252102 (2020).

[36] G. Siegel, Y. P. Venkata Subbaiah, M. C. Prestgard, and A. Tiwari, Growth of centimeter-scale atomically thin $MoS_2$ films by pulsed laser deposition, APL Mater. **3**, 056103 (2015).

[37] H. Sharona, Defects in multilayer $MoS_2$ grown by pulsed laser deposition and their impact on electronic structure, J. Appl. Phys. **130**, 084303 (2021).

[38] W. Muhammad, N. Ullah, M. Haroon, and B. H. Abbasi, Optical, morphological and biological analysis of zinc oxide nanoparticles (ZnO NPs) using: *Papaver somniferum* L, RSC Adv. **9**, 29541 (2019).

[39] Z. Lin, W. Liu, S. Tian, K. Zhu, Y. Huang, and Y. Yang, Thermal expansion coefficient of few-layer $MoS_2$ studied by temperature-dependent Raman spectroscopy, Sci. Rep. **11**, 7037 (2021).

[40] X. Zhang, X. F. Qiao, W. Shi, J. bin Wu, D. S. Jiang, and P. H. Tan, Phonon and Raman scattering of two-dimensional transition metal dichalcogenides from monolayer, multilayer to bulk material, Chem. Soc. Rev. **9**, 2757 (2015).

[41] C. Lee, H. Yan, L. E. Brus, T. F. Heinz, J. Hone, and S. Ryu, Anomalous lattice vibrations of single- and few-layer $MoS_2$, ACS Nano **4**, 2695 (2010).

[42] E. P. Mukhokosi, S. B. Krupanidhi, and K. K. Nanda, Band gap engineering of hexagonal $SnSe_2$ nanostructured thin films for infra-red photodetection, Sci. Rep. **7**, 15215 (2017).

[43] Q. Tian, W. Wu, S. Yang, J. Liu, W. Yao, F. Ren, and C. Jiang, Zinc oxide coating effect for the dye removal and photocatalytic mechanisms of flower-like $MoS_2$ nanoparticles, Nanoscale Res. Lett. **12**, 221 (2017).

[44] H. Henck, Z. B. Aziza, O. Zill, D. Pierucci, C. H. Naylor, M. G. Silly, N. Gogneau, F. Oehler, S. Collin, J. Brault, and F. Sirotti, Interface dipole and band bending in the hybrid $p$-$n$ heterojunction $MoS_2$/GaN(0001), Phys. Rev. B **96**, 115312 (2017).

[45] S. Bag, S. Bhattacharya, D. Dinda, M. v. Jyothirmai, R. Thapa, and S. K. Saha, Induced ferromagnetism and metal-insulator transition due to a charge transfer effect in silver nanoparticle decorated $MoS_2$, Phys. Rev. B **98**, 014109 (2018).

[46] K. M. Freedy, D. H. Olson, P. E. Hopkins, and S. J. McDonnell, Titanium contacts to $MoS_2$ with interfacial oxide: Interface chemistry and thermal transport, Phys. Rev. Mater. **3**, 104001 (2019).

[47] K. L. Kumawat, D. K. Singh, K. K. Nanda, and S. B. Krupanidhi, Solution-processed $SnSe_2$-RGO-based bulk heterojunction for self-powered and broadband photodetection, ACS Appl. Electron. Mater. **3**, 3131 (2021).

[48] S. Qiao, R. Cong, J. Liu, B. Liang, G. Fu, W. Yu, K. Ren, S. Wang, and C. Pan, A vertically layered $MoS_2$/Si heterojunction for an ultrahigh and ultrafast photoresponse photodetector, J. Mater. Chem. C **6**, 3233 (2018).

[49] H. S. Nalwa, A review of molybdenum disulfide ($MoS_2$) based photodetectors: From ultra-broadband, self-powered to flexible devices, RSC Adv. **51**, 30529 (2020).

[50] E. P. Mukhokosi, B. Roul, S. B. Krupanidhi, and K. K. Nanda, Toward a fast and highly responsive $SnSe_2$-based photodiode by exploiting the mobility of the counter semiconductor, ACS Appl. Mater. Interfaces **11**, 6184 (2019).

[51] Y. J. Fang, J. Sha, Z. L. Wang, Y. T. Wan, W. W. Xia, and Y. W. Wang, Behind the change of the photoluminescence property of metal-coated ZnO nanowire arrays, Appl. Phys. Lett. **98**, 33103 (2011).

[52] C. Hu, C. Yuan, A. Hong, M. Guo, T. Yu, and X. Luo, Work function variation of monolayer $MoS_2$ by nitrogen-doping, Appl. Phys. Lett. **113**, 41602 (2018).

[53] S. H. Shen, X. F. Wang, Y. Tian, M. R. Li, Y. Yang, and T. L. Ren, Laser-reconfigured $MoS_2/ZnO$ van der Waals synapse, Nanoscale **11**, 11114 (2019).

[54] Q. Zhao, W. Wang, F. Carrascoso-Plana, W. Jie, T. Wang, A. Castellanos-Gomez, and R. Frisenda, The role of traps in the photocurrent generation mechanism in thin InSe photodetectors, Mater. Horiz. **7**, 252 (2020).

[55] A. M. Chowdhury, G. Chandan, R. Pant, B. Roul, D. K. Singh, K. K. Nanda, and S. B. Krupanidhi, Self-powered, broad band, and ultrafast InGaN-based photodetector, ACS Appl. Mater. Interfaces **11**, 10418 (2019).

[56] See the Supplemental Material at http://link.aps.org/supplemental/10.1103/PhysRevApplied.17.064036 for Figs. S1–S6 (Raman spectra, diffuse reflectance spectra, AFM images of the $MoS_2/ZnO$ heterostructure, $I$-$V$ characteristics, spectral response at different applied biases, and variation of the photoresponse with light-intensity studies).